

# **Simplified Analytical Models for High-Precision Open-Loop Scanning in Atomic Force Microscopy**

Kenichi Umeda<sup>1,2</sup> and Noriyuki Kodera<sup>1</sup>

<sup>1</sup> *Nano Life Science Institute (WPI-NanoLSI),*

*Kanazawa University, Kakuma-machi, Kanazawa, Ishikawa, 920-1192, Japan.*

<sup>2</sup> *PRESTO/JST, 4-1-8 Honcho, Kawaguchi, Saitama 332-0012, Japan.*

## Corresponding Authors

Dr. Kenichi Umeda (E-mail: [umeda.k@staff.kanazawa-u.ac.jp](mailto:umeda.k@staff.kanazawa-u.ac.jp))

Prof. Noriyuki Kodera (E-mail: [nkodera@staff.kanazawa-u.ac.jp](mailto:nkodera@staff.kanazawa-u.ac.jp))

## Abstract

Atomic force microscopy (AFM) enables nanoscale characterization and has been widely applied across diverse systems. In AFM, the tip or sample is typically scanned using piezoelectric scanners, which convert applied voltages into precise mechanical displacements with sub-nanometer accuracy and high bandwidth. However, because piezo elements exhibit nonlinear responses, actual displacements can deviate from the applied driving signal by up to 20–30%. Various methods have been developed to improve positional accuracy, but they often suffer from limited scan speed, increased noise, or complex calibration procedures. From the perspective of routine maintenance, ease of calibration is more advantageous for applications where an error of around 1–2% is acceptable, especially when measuring dynamic molecular motions. Motivated by this, we developed a simple method to generate scan waveforms via software-based feedforward control, which can be easily implemented and calibrated. We identify four distinct sources of positioning error in piezo scanners and demonstrate that these errors can be compensated, achieving more than an order-of-magnitude improvement in positioning accuracy compared with uncompensated operation. Because the proposed method requires no additional hardware and is entirely software-based, it does not deteriorate imaging speed and is compatible with a wide range of AFM systems as well as other scanning probe microscopies.

## 1. Introduction

Atomic force microscopy (AFM) is a versatile nanoscale metrological technique for characterizing surface structures, in which a nanometer-sharp tip is scanned over the sample surface [1-5]. Because AFM is widely used for diverse materials such as electronic devices, polymer materials, and biomolecules [4,6-12], high accuracy in determining structural sizes is essential for reliable measurements. Such accurate analysis is required not only for static structures but also for samples exhibiting rapid dynamics, including biomolecules, which has driven the development of high-speed AFM (HS-AFM) capable of video-rate imaging [9,12-14]. In biomolecular imaging, high accuracy is particularly important for analyzing features closely related to biological functions, such as binding sites and inter-domain distances, angles, or step sizes [14-20]. Consequently, achieving both high-speed imaging and high positional accuracy is necessary.

Piezoelectric scanners—devices that convert applied voltage into mechanical displacement [21]—provide sub-nanometer positional resolution and can be driven at frequencies of tens of kilohertz or higher, making them indispensable for both conventional AFM and HS-AFM [10,12,22,23]. However, nonlinear piezoelectric responses can cause deviations of up to 20–30% between the drive signal and the actual displacement, making compensation necessary [5,12,24].

Closed-loop control, typically implemented using capacitive displacement sensors in AFM instruments, measures the actual piezo displacement in real time and corrects the drive signal accordingly [22,25-27]. Although highly accurate, this approach suffers from sensor noise and limited high-frequency performance, making it unsuitable for HS-AFM. Charge control exploits the more linear relationship between electric charge and displacement in piezo elements and remains effective at high frequencies [28-32], but it suffers from low-frequency drift and leakage and cannot fully compensate for offset-voltage-dependent variations. Both methods also require additional

hardware, increasing system cost.

Model-based feedforward compensation uses hysteresis models to correct nonlinearity without extra hardware [22,33-37]. However, these models often contain many parameters, making parameter identification difficult and limiting their adoption in AFM. Some commercial systems offer simplified hysteresis-compensation modes, but only in a restricted form [38,39]. Moreover, both charge-control and model-based approaches are affected by temperature changes, mechanical stress, or aging, so that calibration may not hold, with possible deviations of a few percent.

Post-image-processing-based hysteresis correction is also widely used [12,24,40-43], but it has several drawbacks: spatial resolution varies with scan location, computational cost is incurred each time data are loaded, periodic or characteristic structures are required, and the backward scan is essential, making it incompatible with scanning strategies that omit the backward pass.

Regardless of the imaging method, regular calibration is essential for achieving high positional accuracy in AFM imaging. However, in many AFM applications, positional errors of 1–2% are often acceptable. Thus, practical factors such as ease of calibration and usability are important, especially in HS-AFM, where high bandwidth and low noise are prioritized. Furthermore, most previous studies have focused solely on hysteresis and dynamic compensation [12,13,36], whereas offset-voltage dependence and scan-size nonlinearity also exert significant influence on positioning errors.

Motivated by these considerations, we first identified four distinct sources of piezo nonlinearity and developed simple analytical compensation models for each, which are both practical and easy to implement. Although designed primarily to improve quantitative distance analysis in molecular AFM imaging, particularly HS-AFM, the method is also applicable to general AFM instruments. Requiring no specialized hardware or complex calibration, the proposed method improves positioning accuracy by more than an order of magnitude, making it useful for a wide range of AFM applications.

## 2. Background of piezo actuator

Ferroelectric materials exhibit spontaneous polarization, the direction of which can be controlled by an external electric field [44]. To reduce internal energy, the polarization is divided into multiple domains rather than being uniform throughout the material. Domain walls are pinned by defects, grain boundaries, and residual stresses, so not all domains readily switch under an average electric field [44,45]. Consequently, displacement increases gradually at low electric fields, rises steeply in the intermediate-field regime due to enhanced domain-wall motion, and saturates at high electric fields as domains become almost fully aligned and domain-wall motion is suppressed. These mechanisms give rise to hysteresis and the characteristic S-shaped displacement–voltage behavior of ferroelectric materials (Fig. 1(a)), which can be approximated by a hyperbolic tangent function.

Because unpoled ferroelectric materials contain randomly oriented domains, their macroscopic piezoelectric response is small. Therefore, piezoelectric elements used in AFM scanners are subjected to a poling process to align the domains in one direction [21]. After poling, the displacement–voltage relationship becomes nearly linear, especially at small voltages (red curve, Fig. 1(b)), where lattice strain dominates. However, at higher voltages, residual microscopic inhomogeneities still allow slight local domain-wall motion, resulting in overall nonlinearity of the displacement–voltage characteristics (blue and green curves, Fig. 1(b)), which degrades positioning accuracy in AFM.

### 3. Methods

In this study, to evaluate piezo nonlinearities, we used a lab-built HS-AFM scanner that adopts an orthogonal XY stack-piezo configuration with a flexure-guided structure, in which the X- and Y-piezo actuators perform the fast and slow scans, respectively (Fig. 1(c)) [13]. Compared with the tube-type piezos commonly used in conventional AFM systems, stack-type piezo actuators offer higher resonance frequencies and relatively lower cross-talk between the XYZ piezos [5,10]. We used commercial piezo actuators (AE0203D08F, NEC Tokin) with a maximum drive voltage of 150 V, a resonance frequency of  $\sim$ 140 kHz. When installed in the scanner and under preload, the resonance frequency was  $\sim$ 40 kHz, and the piezoelectric coefficient was 12–20 nm/V. These actuators are made from hard-piezo material, which provides a wider bandwidth and lower nonlinearity compared with soft-piezo materials.

A waveform generated by computer software and output from a DA converter ( $\pm$ 5 V range) was amplified ten times using a piezo driver (HJPZ-0.1P $\times$ 3, Matsusada Precision Inc., max. 100 V) and applied to the piezo. During the X-scan, an increase in the applied voltage extends the X-piezo, defining the trace (forward) direction, whereas the opposite motion corresponds to the retrace (backward) direction.

For AFM imaging, we employed a typical HS-AFM setup [13], and for actual piezo displacements measurements a heterodyne laser displacement sensor (ST-3761, IWATSU) was used. Frequency sweeps were performed using a frequency response analyzer (FRA5097, NF Corporation).

## 4. Overview of piezo nonlinearity

Through a series of measurements, we classified the nonlinear piezo characteristics affecting AFM positioning accuracy into four major categories, shown in [Table 1](#) and [Fig. 1\(d\)](#):

**Table 1.** Major categories of piezo nonlinearity and their contributions to imaging error

Type of nonlinearity	Imaging error	Contribution order
Tip position (offset voltage) dependency	Max. 30%	1
Scan size nonlinearity	Max. ~25% (typically <15%)	2
Scan wave hysteresis	Max. ~3%	3
Scan frequency	Max. ~1.5%	4

In our measurements, these effects affected the scan size in the order described above. While some commercial instruments include functions to compensate for scan-wave hysteresis via analytical models [[38,39](#)], correcting all four components is uncommon. In the following sections, we describe the characteristics of each effect and the corresponding compensation based on analytical models. In particular, the present study focuses on analyzing and correcting the nonlinearities of the XY piezos.

## 5. Tip position (offset voltage) dependency

In AFM imaging, the largest source of positioning error is the tip position (offset-voltage) dependency described in this section. In molecular AFM imaging, when the molecular density on the substrate is low, a search scan is required to locate the target molecule. Thus, as illustrated in [Fig. 2\(a\)](#), typical AFM control software allows the user to freely adjust the XY tip position. Some commercial AFM systems employ an additional piezo scanner dedicated to sample positioning; however, this approach increases the system size, limits high-speed operation, and raises the overall cost. Therefore, many AFM systems, including our HS-AFM, perform positioning by superimposing an offset voltage onto the scan voltage of the imaging scanner.

However, considering the piezoelectric nonlinearity, the offset voltage may affect the AC piezoelectric coefficient. Therefore, in this section, we evaluate the dependence of the AC piezoelectric coefficient on the offset voltage. As a test specimen, we employed Annexin V two-dimensional (2D) crystals formed on a mica substrate. The 2D crystals were prepared by first spreading a lipid membrane on mica and subsequently coating the surface with Annexin V [\[12,16,46\]](#).

Imaging was first performed near the center of the positioning range (XY offset voltage = 50 V). The image size was  $200 \times 200$  nm, corresponding to  $\sim 13$  V, or 13% of the maximum voltage. A Fourier filter was applied to the image to subtly enhance the periodic structure. In [Fig. 2\(b\)](#), Clear hexagonal 2D lattices of Annexin V exhibiting six-fold symmetry were observed. The XY piezo constants were calibrated at this position so that the lattice constant of Annexin V matched the theoretical value of 17.7 nm [\[16,46\]](#).

Next, as shown in [Fig. 2\(c\)](#), imaging was performed at the upper-right edge of the positioning range (XY offset voltage  $\approx 92$  V), where the lattice constant was observed to be  $\sim 22.3$  nm ( $\approx 25\%$  increase). In contrast, as shown in [Fig. 2\(d\)](#), at the lower-left edge (XY offset voltage  $\approx 8$  V), the

lattice constant decreased to  $\sim 16.3$  nm ( $\approx 8\%$  decrease). These results indicate that the scan range can differ by up to  $\sim 30\%$  between the negative and positive ends. As shown in Fig. 2(e), the required modulation depth  $m$  of the scan-waveform amplitude to recover the correct lattice constant exhibited a nonlinear dependence and increased steeply at larger offset voltages.

This behavior can be explained as follows. In AFM piezo scanners, ferroelectric domains are pre-aligned by poling, producing macroscopic polarization even at 0 V. Applying a DC offset reduces the contribution of movable domain walls, lowering the local slope of the displacement–electric field curve and decreasing the AC piezoelectric coefficient. This effect is more pronounced in flexure-guided scanners, where the mechanical load on the piezo element increases with displacement [12,22,23]. As a result, the actual AC displacement is smaller for a given voltage, making the molecular lattice appear artificially enlarged.

To compensate for this effect by adjusting the gain of the scan signal,  $m$  is approximated by the following quadratic function:

$$m = 1 + \alpha_{\text{offset}} p_{\text{offset}} + \beta_{\text{offset}} p_{\text{offset}}^2, \quad (1)$$

where the coefficients  $\alpha_{\text{offset}}$  and  $\beta_{\text{offset}}$  correspond to the linear and quadratic terms, respectively.  $p_{\text{offset}}$  represents the normalized XY offset voltage, scaled to the range  $-1$  to  $+1$ , which can be expressed by

$$p_{\text{offset}} = 2 \frac{V_{\text{offset}}}{V_{\text{Max}}} - 1, \quad (2)$$

where  $V_{\text{offset}}$  and  $V_{\text{Max}}$  denote the applied offset voltage and the maximum output voltage of the piezo driver (100 V in our setup), respectively. As these equations indicate,  $m = 1$  at the center of the positioning range ( $V_{\text{offset}} = 50$  V and  $p_{\text{offset}} = 0$ ). Let  $m_-$  and  $m_+$  denote the values of  $m$  at  $p_{\text{offset}} = -1$  and  $p_{\text{offset}} = +1$ , respectively. The coefficients  $\alpha_{\text{offset}}$  and  $\beta_{\text{offset}}$  in Eq. (1) can then be determined as:

$$\alpha_{\text{offset}} = \frac{m_+ - m_-}{2} \quad \text{and} \quad (3)$$

$$\beta_{\text{offset}} = \frac{m_+ + m_-}{2} - 1. \quad (4)$$

Thus, the user first calibrates the XY piezo constants by imaging a calibration sample at the center of the positioning range. Next, imaging is performed near the negative and positive ends of the X positioning range to determine  $m_-$  and  $m_+$ , from which  $\alpha_{\text{offset}}$  and  $\beta_{\text{offset}}$  can be obtained. Since measurement errors are minimized among the three calibration points, it is preferable to perform calibration at positions slightly away from the extreme edges rather than exactly at the edges. The same procedure is applied to the Y direction, enabling correct scan sizes to be set at any position within the XY range. Tests on various piezo scanners showed that  $m_+ = 1.2\text{--}1.3$  and  $m_- = 0.85\text{--}0.95$ , and only a slight dependence on piezo size was observed.

## 6. Scan size nonlinearity

In AFM measurements, scan sizes are adjusted depending on whether the scan is for searching or high-resolution imaging and optimized for the target molecular size. Therefore, it is important to ensure that quantitative distance measurements can be performed across a range of scan sizes.

The AC voltage of the scan signal applied to the piezo,  $V_{\text{scan}}$ , is typically calculated from the user-defined scan range,  $R_{\text{scan}}$ , assuming linearity between scan size and voltage, as follows:

$$R_{\text{scan}} = k_{\text{scan}} V_{\text{scan}}, \quad (5)$$

where  $k_{\text{scan}}$  represents the linearly approximated piezoelectric coefficient.

However,  $R_{\text{scan}}$  is not strictly linear with respect to  $V_{\text{scan}}$ . For example, as shown in [Fig. 3\(a\)](#), Annexin V was imaged at a scan size of  $200 \times 200 \text{ nm}^2$ , and the scanner was calibrated so that the lattice constant matched the ideal value. Under this calibrated condition, imaging at  $390 \times 390 \text{ nm}^2$  resulted in an observed lattice constant of 16.4 nm, approximately 8% smaller ([Fig. 3\(b\)](#)).

This behavior arises because, even in poled piezo elements, the displacement–electric field characteristics are not strictly linear. As the AC voltage increases, reversible domain-wall motion and rotation of non- $180^\circ$  domains are activated. As a result, the displacement amplitude increases nonlinearly with the electric-field amplitude, and the effective AC piezoelectric coefficient increases with increasing AC voltage.

To evaluate this quantitatively, we measured the AC voltage dependence of the piezo displacement using a laser displacement sensor. As shown in [Fig. 3\(c\)](#), the displacement exhibited a nonlinear relationship, with a smaller slope at low voltages and a steeper slope at high voltages. [Figure 3\(d\)](#) shows the deviation from a linear approximation assuming calibration was performed at 200 nm. As seen, small scan sizes exhibited errors of up to  $\sim 7\%$ , whereas large scan sizes can show deviations of up to  $\sim 25\%$ .

Based on these results, we adopted the following quadratic expression to describe the scan size:

$$R_{\text{scan}} = \alpha_{\text{scan}} V_{\text{scan}} (1 + \beta_{\text{scan}} V_{\text{scan}}), \quad (6)$$

where  $\alpha_{\text{scan}}$  and  $\beta_{\text{scan}}$  represent the scaling factor and nonlinear factor of the piezoelectric coefficient, respectively.  $\beta_{\text{scan}} = 0$  corresponds to a perfectly linear response, and its typical values range from about 0.5 to 1.5.

To perform calibration based on this quadratic function, users only need to set  $k_{\text{scan}}$  and  $\beta_{\text{scan}}$  in the software during calibration, while  $\alpha_{\text{scan}}$  is automatically determined as an internal parameter as follows.

$$\alpha_{\text{scan}} = \frac{k_{\text{scan}}}{1 + \beta_{\text{scan}} \frac{R_{\text{base}}}{k_{\text{scan}}}}. \quad (7)$$

First, the calibration sample is imaged to determine the optimal  $k_{\text{scan}}$  at a base scan size  $R_{\text{base}}$ , using the frame rate and pixel numbers typically used for imaging. Because the scan accuracy is highest near the chosen  $R_{\text{base}}$ , it is preferable to select a scan size that is most frequently used. For biomolecular imaging, a typical  $R_{\text{base}}$  is  $200 \times 200 \text{ nm}^2$ . The initial value of  $\beta_{\text{scan}}$  is set to the typical range indicated above. The  $k_{\text{scan}}$  determined at this stage is compatible with a conventional system that assumes a linear piezo coefficient.

Subsequently, the scan size is changed to a value different from  $R_{\text{base}}$ , for example  $600 \times 600 \text{ nm}^2$ , and  $\beta_{\text{scan}}$  is further optimized. The frame rate is adjusted to maintain the same scan velocity as at  $R_{\text{base}}$ . This calibration procedure enables the determination of both  $\alpha_{\text{scan}}$  and  $\beta_{\text{scan}}$ . Although the scan accuracy is maximized at the two scan sizes used for calibration, extrapolation of the quadratic function of Eq. (6) to other scan ranges allows high scan accuracy to be maintained over a broader range of scan sizes than with a linear approximation.

To implement this method in software, it is necessary to calculate  $V_{\text{scan}}$  from  $R_{\text{scan}}$  specified in the software. By solving Eq. (6) for  $V_{\text{scan}}$ , the corresponding  $V_{\text{scan}}$  for a given  $R_{\text{scan}}$  can be obtained analytically as follows:

$$V_{\text{scan}} = \frac{1}{2\beta_{\text{scan}}} \left( \sqrt{1 + \frac{4\beta_{\text{scan}} R_{\text{scan}}}{\alpha_{\text{scan}}}} - 1 \right). \quad (8)$$

Introducing this quadratic correction alone already allows for higher positional accuracy compared with the conventional linear approximation. However, as shown in [Fig. 3\(e\)](#), the experimental result showed that at large scan sizes, the slope becomes slightly shallower than that predicted by the quadratic function. Consequently, approximating the entire scan range with a quadratic function can result in deviations of up to 6% at large scan ranges. One possible solution is to use a cubic function; however, unlike the quadratic function, the cubic function does not allow an exact analytical inverse to be obtained.

Therefore, we adopted a hybrid approach: for voltages below a set threshold  $V_{\text{th}}$ , the quadratic function given in [Eq. \(6\)](#) is used, while for voltages above  $V_{\text{th}}$ , a linear extrapolation of the quadratic function is employed as follows:

$$R_{\text{scan}} = \alpha_{\text{scan}} \left[ (1 + 2\beta_{\text{scan}} V_{\text{th}}) V_{\text{scan}} - \beta_{\text{scan}} V_{\text{th}}^2 \right] \quad \text{for } V_{\text{scan}} > V_{\text{th}}. \quad (9)$$

The corresponding scan size  $R_{\text{th}}$  at the threshold  $V_{\text{th}}$  is given by:

$$R_{\text{th}} = \alpha_{\text{scan}} V_{\text{th}} (1 + \beta_{\text{scan}} V_{\text{th}}). \quad (10)$$

Furthermore, the inverse of [Eq. \(9\)](#) can be solved analytically as shown below, facilitating straightforward software implementation:

$$V_{\text{scan}} = \frac{R_{\text{scan}} + \alpha_{\text{scan}} \beta_{\text{scan}} V_{\text{th}}^2}{\alpha_{\text{scan}} (1 + 2\beta_{\text{scan}} V_{\text{th}})} \quad \text{for } V_{\text{scan}} > V_{\text{th}}. \quad (11)$$

In our case, the typical threshold voltage was found to be  $V_{\text{th}} \approx 50$  V. With this correction, as shown in [Fig. 3\(f\)](#), higher-accuracy positional control can be maintained across the entire scan range.

## 7. Scan wave hysteresis

In piezo scanners, the displacement–voltage relationship is relatively linear at small AC voltages, whereas at large AC voltages it becomes nonlinear due to significant domain-wall motion (Fig. 1b). Because this motion lags behind the applied voltage, the nonlinearity is accompanied by hysteresis [5,21,44,47]. In this section, we describe an analytical compensation model for this hysteretic behavior.

In typical AFM imaging, a triangular waveform is used as the scan signal, which can be expressed as follows:

$$V(t) = V_{\text{scan}} f(t), \quad (12)$$

where the dimensionless function  $f(t)$  is defined as:

$$f(t) = \begin{cases} \frac{t}{\alpha_{\text{turn}}} & \text{for } 0 < t \leq \alpha_{\text{turn}}, \\ 1 - \frac{t - \alpha_{\text{turn}}}{1 - \alpha_{\text{turn}}} & \text{for } \alpha_{\text{turn}} < t \leq 1, \end{cases} \quad (13)$$

where  $t$  represents the normalized time of a single line-scan period, and  $\alpha_{\text{turn}}$  denotes the turning point between forward and backward scans.

For a standard triangular-wave X-scan,  $\alpha_{\text{turn}} = 0.5$ . This expression can also be applied to a sawtooth-like wave ( $\alpha_{\text{turn}} > 0.5$ ), which is used to increase imaging speed: images are acquired during the forward scan, while the backward scan is skipped by temporarily lifting the probe from the sample surface [48,49]. For Y-scans, a triangular wave ( $\alpha_{\text{turn}} = 0.5$ ) is typically used, with images acquired in both directions. However, this approach can cause frame-to-frame shifts in molecular shape and position, as the direction of drift-induced image distortion is opposite between forward and backward scans. To mitigate this, a sawtooth-like wave ( $\alpha_{\text{turn}} \approx 1$ ) is often employed.

The hysteresis of the piezo scanner was characterized using a laser displacement sensor.

Application of a  $\sim 90$  V triangular waveform (top, Fig. 4(a)) produced a delayed strain response (middle, Fig. 4(a)), causing the right half of images to appear laterally stretched (bottom, Fig. 4(a)). This distortion can be compensated by applying a nonlinear waveform incorporating the inverse hysteresis transfer function (top, Fig. 4(b)), restoring near-linear piezo behavior (middle, Fig. 4(b)) and producing distortion-free images (bottom, Fig. 4(b)).

However, applying high-frequency scan waveforms to the X piezo can excite its resonances, resulting in vertical streaks (ringing) in AFM images. To prevent this, suppression of high-frequency components is essential [10,13]. This can be readily achieved in software by applying a low-pass filter to the analytical solution in the Fourier domain during waveform generation, enabling sharp filtering and flexible cutoff frequencies. This implementation is also crucial for inverse-compensation-based damping [12,13,36].

To achieve both of these characteristics and facilitate calibration, we adopted an analytical approximation method that uses a functional form reproducing the nonlinear piezo hysteresis. For example, when the hysteresis characteristic is approximated by a quadratic function, it can be expressed as:

$$x = \alpha_{\text{hyst}} (V / V_{\text{scan}}) + \beta_{\text{hyst}} (V / V_{\text{scan}})^2, \quad (14)$$

where  $x$  denotes the normalized piezo displacement. The inverse transfer characteristic can be obtained by solving this equation for  $V$ . Furthermore, we substitute  $x = t$  to make  $x$  vary linearly with time  $t$ , yielding the following expression:

$$V(t) = V_{\text{scan}} \frac{\sqrt{4\alpha_{\text{hyst}} t + \beta_{\text{hyst}}^2} - \beta_{\text{hyst}}}{2\alpha_{\text{hyst}}}. \quad (15)$$

Although this method is intuitive, the Fourier transform of this equation cannot be obtained exactly because it contains a square-root term.

We next take an analytical model in which a sine wave is superimposed on a triangular waveform [41], expressed as:

$$f(t) = \begin{cases} \frac{t}{\alpha_{\text{turn}}} + \beta_1 \sin\left(\pi \frac{t}{\alpha_{\text{turn}}}\right) & \text{for } 0 < t \leq \alpha_{\text{turn}}, \\ 1 - \frac{t - \alpha_{\text{turn}}}{1 - \alpha_{\text{turn}}} - \beta_2 \sin\left(\pi \frac{t - \alpha_{\text{turn}}}{1 - \alpha_{\text{turn}}}\right) & \text{for } \alpha_{\text{turn}} < t \leq 1, \end{cases} \quad (16)$$

where  $\beta_1$  and  $\beta_2$  represent the nonlinear factors of the forward and backward scan waveforms, respectively. This model is referred to as the “sinusoidal model.” These equations can be exactly Fourier-transformed ([Supplementary Material](#)), making it directly applicable to AFM scan waveforms.

For comparison, prior to examining the nonlinear compensation, we experimentally measured the piezo displacement induced by a triangular waveform. To compare the forward and backward scans, the backward waveform was horizontally flipped and plotted alongside the forward data on the same graph ([Fig. 4\(c, left\)](#)). The figure shows that, in both curves, the center of the bulging is located near the midpoint of the x-axis (see arrow). In addition, the bulging amplitude in the backward scan is approximately twice that in the forward scan, which is an intrinsic characteristic of flexure-guided scanners.

[Figure 4\(d, left\)](#) compares the input triangular waveform with the resulting piezo displacement. To quantitatively evaluate the deviation from an ideal triangular waveform, the difference between the two is plotted in [Fig. 4\(e, left\)](#). As shown, the maximum deviations from linearity under triangular input are approximately 3% and 7% for the forward and backward scans, respectively. Thus, the nonlinearity in the backward scan is confirmed to be approximately twice as large as that in the forward scan.

Next, scan waveforms were generated using the sinusoidal model. The inverse transfer characteristic of [Eq. \(16\)](#) was calculated, and  $t$  was substituted with  $x$  for plotting ([Fig. 4\(c, middle\)](#)). It was observed that line bulging increased with the nonlinear factor. However, unlike the experimental results, the bulging was asymmetric, with pronounced nonlinearity around  $x \approx 0.8$ . To quantify the deviation from an ideal triangular waveform, the nonlinear factors were optimized so

that the scanner displacement became as close to linear as possible. As a result, the error from the triangular waveform was estimated to be approximately  $\pm 1.8\%$  (Fig. 4(d,e, middle)).

To further approach an ideal triangular waveform, we developed an analytical model of a nonlinear waveform with higher symmetry. Investigation showed that exponential functions preserve symmetry while allowing Fourier transformation, as follows.

$$f(t) = \begin{cases} \frac{1 - \exp\left(-\frac{\beta_1}{\alpha_{\text{turn}}} t\right)}{1 - \exp(-\beta_1)} & \text{for } 0 < t \leq \alpha_{\text{turn}}, \\ 1 - \frac{1 - \exp\left[-\beta_2 \left(\frac{t - \alpha_{\text{turn}}}{1 - \alpha_{\text{turn}}}\right)\right]}{1 - \exp(-\beta_2)} & \text{for } \alpha_{\text{turn}} < t \leq 1. \end{cases} \quad (17)$$

This model is referred to as the “exponential model,” and the resulting waveform is shown in Fig. 4(c, right). Although minor asymmetry remains, the waveform is significantly more symmetric than that in Fig. 4(c, middle), and the error is suppressed to approximately 1% (Fig. 4(d,e, right)).

Next, the scan-size dependence of the nonlinear factors was investigated. Nonlinear waveforms generated using the exponential model were applied to the piezo, and the nonlinear factor was optimized to achieve the most linear response. The resulting factors were plotted against scan size (Fig. 4(f)). As shown, the nonlinearity factor increases with scan size; however, at larger scan sizes, this trend saturates, resulting in a more gradual dependence.

Finally, we describe the specific software implementation. By measuring the nonlinear factors at only some representative scan sizes and tabulating them, the nonlinear factor at any arbitrary scan size can be obtained through polynomial interpolation. Alternatively, we found that empirical formulas can fit the experimental data; for example, the curves were well approximated by the following equation (green dashed line in Fig. 4(f)):

$$\beta_x = \gamma \tilde{R}_{\text{scan}}^{\frac{1}{2} - \frac{\tilde{R}_{\text{scan}}}{4}}, \quad (18)$$

where  $\tilde{R}_{\text{scan}}$  denotes the normalized  $R_{\text{scan}}$  defined as follows:

$$\tilde{R}_{\text{scan}} = \frac{R_{\text{scan}}}{R_{\text{Max}}}. \quad (19)$$

Because hysteresis increases not only with drive amplitude but also with frequency [26,33], it is preferable to perform calibration at a slightly lower scan frequency than the one typically used to avoid over-compensation. Although hysteresis grows with scan size, it remains minimal for the small scan ranges typical of molecular imaging. Furthermore, in HS-AFM systems using stack-type piezo scanners, forward-scan nonlinearities are roughly half those of the backward scan; therefore, using forward-scan data for quantitative structural analysis helps minimize analytical errors.

## 8. Scan frequency

In AFM imaging, the frame rate must be adjusted according to the dynamical behavior and fragility of the sample. However, the apparent AC piezoelectric coefficient exhibits frequency dependence. For example, as shown in [Fig. 5\(a\)](#), Annexin V was imaged at a scan size of  $100 \times 100 \text{ nm}^2$  and 0.5 fps, and the scanner was calibrated under this condition so that the lattice constant became 17.7 nm. When the frame rate was subsequently increased by a factor of 14 to 7.3 fps, the apparent lattice constant increased to 18.3 nm, corresponding to a 3% increase ([Fig. 5\(b\)](#)).

This is due to “creep,” a phenomenon in which displacement gradually increases after an applied voltage change [[5,21,24,44,47](#)]. Creep arises from delayed domain-wall motion caused by pinning and crystal structural inhomogeneities. Consequently, the apparent molecular size increases with increasing frame rate.

To evaluate this effect quantitatively, the frequency response of the X scanner was measured by sweeping the frequency of the applied triangular waveform using a frequency response analyzer. As shown in [Fig. 5\(c\)](#), the response was nearly flat at low frequencies, but resonance peaks appeared above approximately 10 kHz. However, when the vertical axis is expanded ([Fig. 5\(d\)](#)), a slight decrease in gain with frequency is observed even in the low-frequency range. This behavior was well reproduced using the following empirical formula:

$$R_{\text{scan}} = \left( 1 + \frac{f_{\text{scan}}}{f_{\text{creep}}} \right)^{-\alpha_{\text{creep}}/2}, \quad (20)$$

where  $f_{\text{scan}}$  is the scan frequency,  $f_{\text{creep}}$  is the creep cutoff frequency, and  $\alpha_{\text{creep}}$  represents the frequency dependence of the creep. Typical values were  $f_{\text{creep}} = 0.2 \text{ Hz}$  and  $\alpha_{\text{creep}} = 0.03$ .

Under the condition  $f_{\text{scan}} \gg f_{\text{creep}}$ , [Eq. \(19\)](#) can be approximated by a Taylor expansion as follows:

$$R_{\text{scan}} \approx C_{\text{creep}} - \alpha_{\text{creep}} \log_{10} \left( 2 \frac{f_{\text{scan}}}{f_{\text{creep}}} \right), \quad (21)$$

where  $C_{\text{creep}}$  is a constant approximately equal to 1. From this equation,  $\alpha_{\text{creep}}$  indicates the ratio of reduction in effective scan range for a tenfold increase in frequency; for instance,  $\alpha_{\text{creep}} = 0.03$  corresponds to a  $\sim 3\%$  decrease per decade. This frequency dependence showed no significant voltage dependence.

Calibration of scan hysteresis and scan-frequency dependence requires a laser displacement sensor, which is generally unavailable in laboratories that do not develop AFM instruments. However, because the scan speed is typically adjusted only within a factor of two to three, frequency-dependent errors remain below approximately 1.5%. Furthermore, tests on multiple piezo scanners showed no significant differences, suggesting that typical values can be used as common parameters.

## 9. Nonlinearity in Z-scanner

Similar to the XY scanner, the Z scanner exhibits piezoelectric nonlinearity and can contribute to errors in height analysis. However, because the Z scanner operates under feedback control during AFM imaging, feedforward compensation is impractical. Nevertheless, for the reasons described below, the nonlinearity of the Z scanner is often less critical than that of the XY scanner.

Unlike XY scanners, the Z scanner has an open-ended structure and is therefore subject to minimal mechanical loading. Moreover, in typical AFM measurements, approaching the limits of the Z-scanner travel range may prevent image acquisition or risk tip–sample crash; therefore, measurements are performed near the center of the travel range. As a result, the offset-voltage dependence, which strongly contributes to piezoelectric nonlinearity, is much smaller for the Z scanner.

In addition, during practical imaging, the Z scanner is operated over a limited displacement range, typically well below half of its maximum travel. This operating condition effectively suppresses the piezo hysteresis and scan-size nonlinearity. Because molecular imaging generally requires only a small Z range, a maximum piezo-driver voltage of approximately 50 V is sufficient, corresponding to less than one-third of the maximum voltage of the piezo element (~150 V). Under these conditions, measurement errors arising from Z-scanner nonlinearity can be further reduced. This approach is also effective for the XY piezo scanner in improving positioning accuracy.

## 10. Conclusions

In this study, we identified four types of nonlinear effects in open-loop piezo AFM scanners and experimentally assessed their impact on positioning errors. We proposed simple analytical models to compensate for these effects, achieving high-precision control without specialized hardware. Software-based correction preserves scanner bandwidth and noise characteristics, maintaining compatibility with existing systems. For high-resolution imaging, tip-position (offset voltage) dependence and scan-size nonlinearity are the most significant, and compensating for these two alone is sufficient. These two effects can be easily calibrated using standard imaging-based procedures. The method developed in this study has already been applied to practical biomolecular imaging experiments [18-20,50], providing a valuable tool for analyzing biomolecular dynamics. This method is applicable not only to stack-type piezos but also to tube piezos and is therefore suitable for other common scanning probe microscopies as well.

## **Acknowledgements**

We thank Professor Toshio Ando of Kanazawa University and Dr. Takashi Morii of RIBM Co., Ltd. for their valuable support, and the technical assistants Ms. Aimi Makino and Ms. Kayo Nakatani for calibrating the piezo scanners. This work was supported by PRESTO, Japan Science and Technology Agency (JST) [JPMJPR20E3 and JPMJPR23J2 to K.U.]; and KAKENHI, Japan Society for the Promotion of Science [25K09575 (to K.U.), and 24H00402 (to N.K.)].

## **Author contributions**

K. U. constructed the theories, performing the experiments, and wrote the manuscript; and N. K. supervised the study.

## Figures

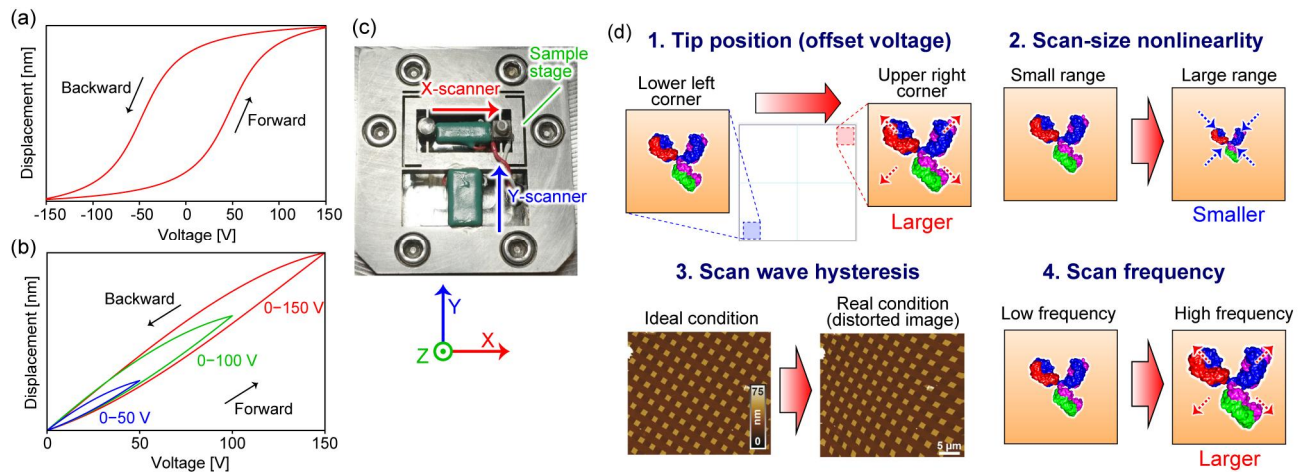


**FIG. 1. (a,b)** Schematics of displacement–voltage characteristics for (a) an unpoled piezo element and (b) a poled piezo element. In (b), the curves for voltage ranges of 50, 100, and 150 V are shown, indicating that both nonlinearity and hysteresis increase with increasing voltage. **(c)** Appearance of the HS-AFM scanner used in the experiments. **(d)** Schematics illustrating the four types of nonlinearities in piezo actuators. To clearly illustrate differences in the actual AFM scan size, an electron-density isosurface generated from an IgG2a monoclonal antibody (PDB: 1IGT) was used as a model molecule for schematic purposes. The two AFM images at the lower left in (d) are adapted from A. Marchesi et al., *Scientific Reports* (2021), licensed under CC BY 4.0 [12].

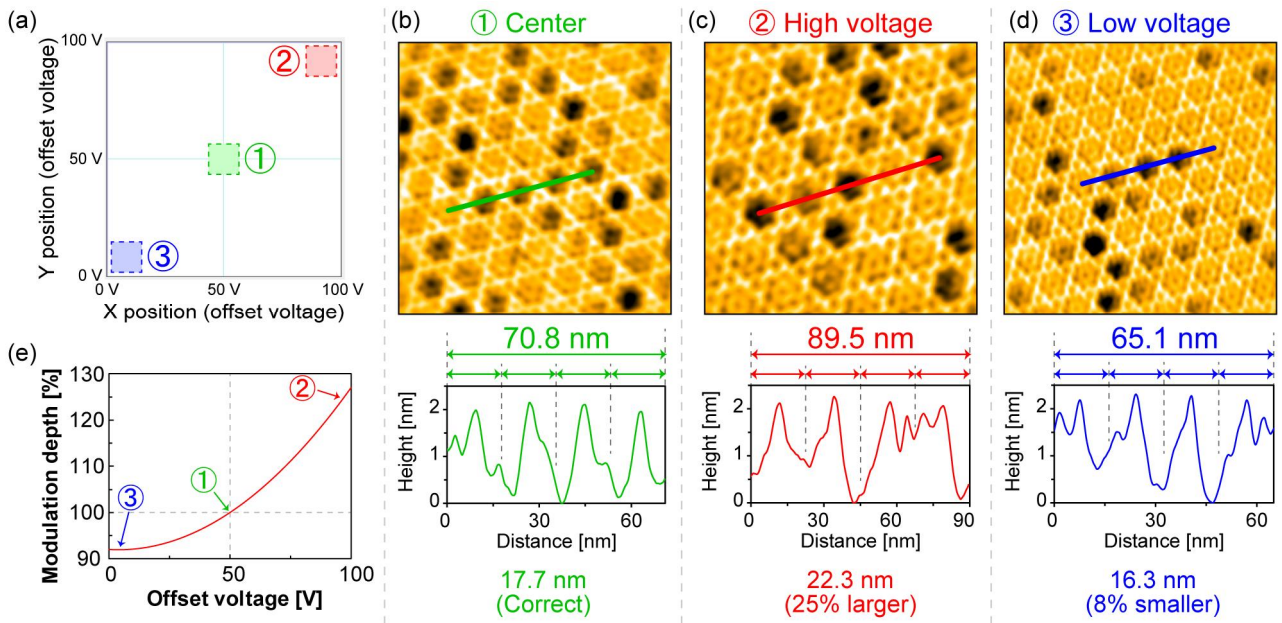


**FIG. 2.** (a) Control of the XY tip position (offset voltage) in an AFM software. (b-d) Tip-position dependence of AFM images of the Annexin V 2D crystal: center (b), upper right (c), and lower left (d). The upper panels show the AFM images, and the lower panels display the line profiles taken along the lines indicated in the AFM images. AFM images were acquired at each location with a nominal scan size of  $200 \times 200 \text{ nm}^2$  and are shown as magnified views of  $130 \times 130 \text{ nm}^2$ . The frame rate was 1.8 fps. (e) Dependence of the modulation depth required to accurately determine the lattice constant on the offset voltage.

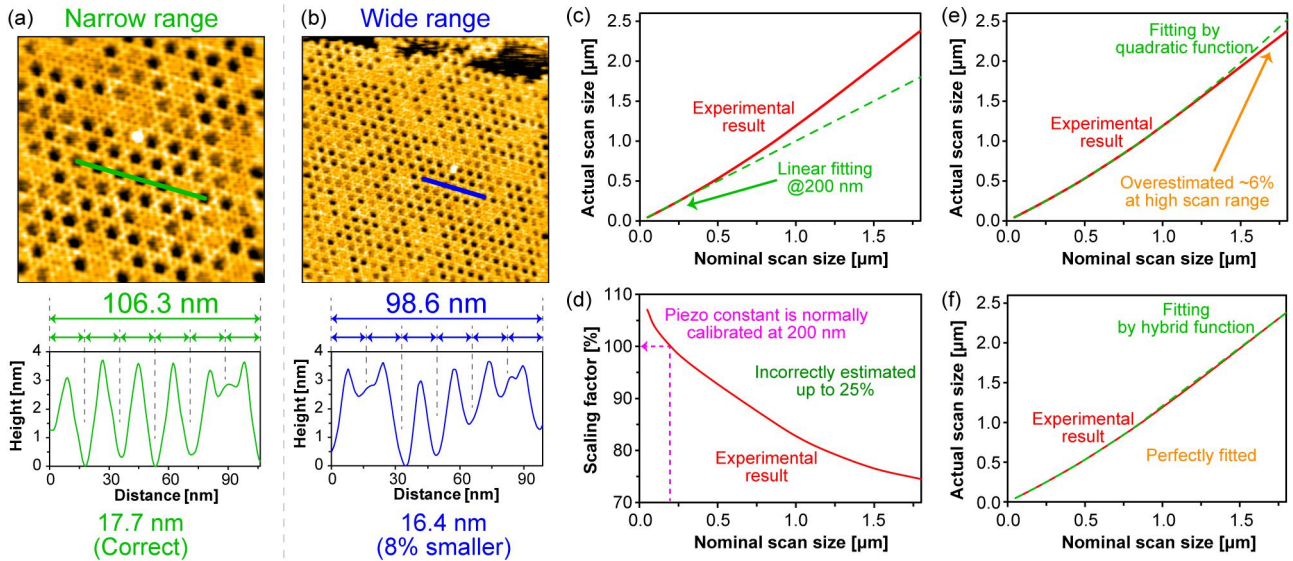


**FIG. 3.** (a,b) Scan-size dependence of AFM images of the Annexin V 2D crystal with a small (a,  $200 \times 200 \text{ nm}^2$ , 1.8 fps) and a large (b,  $390 \times 390 \text{ nm}^2$ , 0.7 fps) scan sizes. The upper panels show the AFM images, and the lower panels display the line profiles taken along the lines indicated in the AFM images. (c) Correlation between the nominal scan size, set under the assumption of a linear piezoelectric coefficient, and the actual scan size determined by the laser displacement sensor. (d) Scan-size dependence of the scaling factor required to obtain the correct scan size. (e) Comparison of the scan size obtained from the quadratic model with the experimental results. (f) Comparison of the scan size obtained from the hybrid linear–quadratic model with the experimental results.

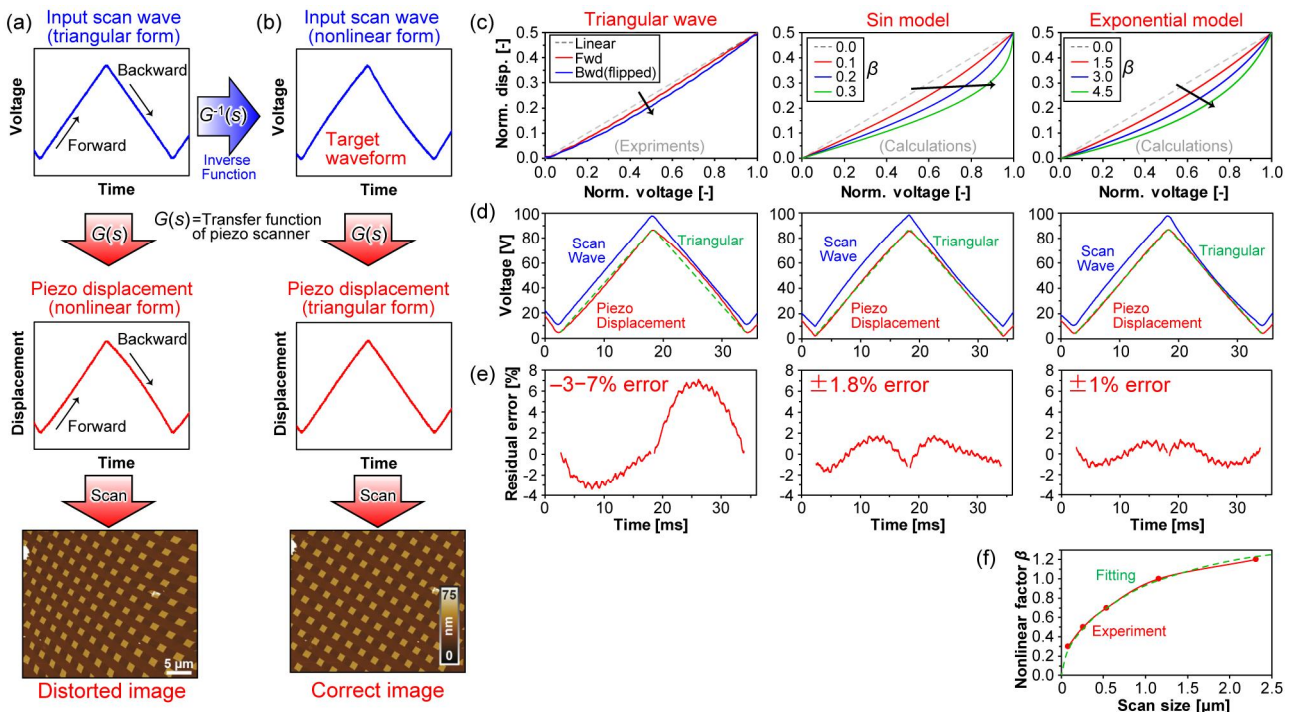


**FIG. 4. (a,b)** Dependence of piezo displacement and AFM images on the scan waveform: top, input scan waveforms; middle, resulting piezo displacements; bottom, AFM images. A standard triangular input causes nonlinear displacement and image distortion (a), whereas an inverse-corrected waveform restores a triangular displacement and eliminates the distortion (b). In the triangular waveform, the initial rising and subsequent falling segments represent the forward and backward scans, respectively. The two AFM images at the bottom are adapted from A. Marchesi et al., Scientific Reports (2021), licensed under CC BY 4.0 [12]. **(c)** Comparison of the forward and backward piezo responses obtained experimentally with a triangular input (left), and the dependence of the nonlinear waveforms on the nonlinear factor for the sinusoidal model (middle) and exponential model (right). **(d,e)** Piezo displacement responses obtained using the triangular, sinusoidal-model, and exponential-model input waveforms (d), and their residuals from the ideal triangular waveform (e). **(f)** Scan-size dependence of the optimal nonlinear factor for the exponential model of X piezo in the forward scan.

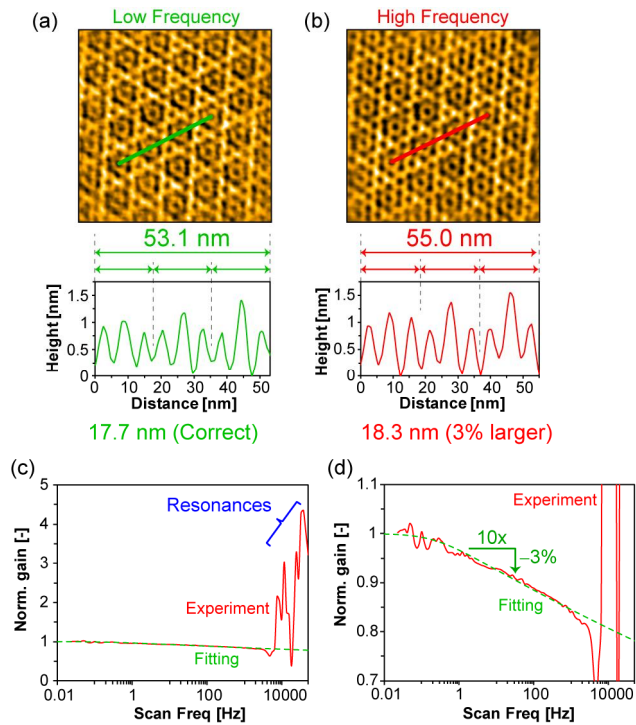


**FIG. 5. (a,b)** Scan-frequency dependence of AFM images of the Annexin V 2D crystal at low (a, 0.5 fps) and high (b, 7.3 fps) imaging rates. The upper panels show the AFM images, and the lower panels display the line profiles taken along the lines indicated in the AFM images. Both of the images were acquired at a nominal scan size of  $100 \times 100 \text{ nm}^2$ . **(c,d)** Frequency dependence of the piezo AC response obtained by sweeping the input triangular-wave frequency at an AC voltage of 20 V<sub>p-0</sub> (c) and a magnified view of the data (d).

## References

- [1] G. Binnig, C. F. Quate, and C. Gerber, Atomic Force Microscope, *Phys. Rev. Lett.* **56**, 930 (1986).
- [2] R. Garcia and R. Perez, Dynamic atomic force microscopy methods, *Surf. Sci. Rep.* **47**, 197 (2002).
- [3] F. J. Giessibl, Advances in atomic force microscopy, *Rev. Mod. Phys.* **75**, 949 (2003).
- [4] Y. F. Dufrêne, T. Ando, R. Garcia, D. Alsteens, D. Martinez-Martin, A. Engel, C. Gerber, and D. J. Müller, Imaging modes of atomic force microscopy for application in molecular and cell biology, *Nat. Nanotechnol.* **12**, 295 (2017).
- [5] H. Habibullah, 30 Years of atomic force microscopy: Creep, hysteresis, cross-coupling, and vibration problems of piezoelectric tube scanners, *Measurement* **159**, 107776 (2020).
- [6] V. V. Korolkov, A. Summerfield, A. Murphy, D. B. Amabilino, K. Watanabe, T. Taniguchi, and P. H. Beton, Ultra-high resolution imaging of thin films and single strands of polythiophene using atomic force microscopy, *Nat. Commun.* **10**, 1537 (2019).
- [7] A. F. Payam and A. Passian, Imaging beyond the surface region: Probing hidden materials via atomic force microscopy, *Sci. Adv.* **9**, eadg8292 (2023).
- [8] S. Chioldini, J. Kerfoot, G. Venturi, S. Mignuzzi, E. M. Alexeev, B. T. Rosa, S. Tongay, T. Taniguchi, K. Watanabe, A. C. Ferrari, and A. Ambrosio, Moiré Modulation of Van Der Waals

Potential in Twisted Hexagonal Boron Nitride, *ACS Nano* **16**, 7589 (2022).

[9] A. P. Nievergelt, N. Banterle, S. H. Andany, P. Gonczy, and G. E. Fantner, High-speed photothermal off-resonance atomic force microscopy reveals assembly routes of centriolar scaffold protein SAS-6, *Nat. Nanotechnol.* **13**, 696 (2018).

[10] A. P. Nievergelt, B. W. Erickson, N. Hosseini, J. D. Adams, and G. E. Fantner, Studying biological membranes with extended range high-speed atomic force microscopy, *Sci. Rep.* **5**, 11987 (2015).

[11] S. Datta, Y. Kato, S. Higashiharaguchi, K. Aratsu, A. Isobe, T. Saito, D. D. Prabhu, Y. Kitamoto, M. J. Hollamby, A. J. Smith, R. Dagleish, N. Mahmoudi, L. Pesce, C. Perego, G. M. Pavan, and S. Yagai, Self-assembled poly-catenanes from supramolecular toroidal building blocks, *Nature* **583**, 400 (2020).

[12] A. Marchesi, K. Umeda, T. Komekawa, T. Matsubara, H. Flechsig, T. Ando, S. Watanabe, N. Kodera, and C. M. Franz, An ultra-wide scanner for large-area high-speed atomic force microscopy with megapixel resolution, *Sci. Rep.* **11**, 13003 (2021).

[13] T. Ando, T. Uchihashi, and T. Fukuma, High-speed atomic force microscopy for nano-visualization of dynamic biomolecular processes, *Prog. Surf. Sci.* **83**, 337 (2008).

[14] T. Ando, T. Uchihashi, and S. Scheuring, Filming Biomolecular Processes by High-Speed Atomic Force Microscopy, *Chem. Rev.* **114**, 3120 (2014).

[15] J. Preiner, N. Kodera, J. L. Tang, A. Ebner, M. Brameshuber, D. Blaas, N. Gelbmann, H. J.

Gruber, T. Ando, and P. Hinterdorfer, IgGs are made for walking on bacterial and viral surfaces, *Nat. Commun.* **5**, 4394 (2014).

- [16] A. Miyagi, C. Chipot, M. Rangl, and S. Scheuring, High-speed atomic force microscopy shows that annexin V stabilizes membranes on the second timescale, *Nat. Nanotechnol.* **11**, 783 (2016).
- [17] H. Imai, T. Uchiumi, and N. Kodera, Direct visualization of translational GTPase factor pool formed around the archaeal ribosomal P-stalk by high-speed AFM, *Proc. Natl. Acad. Sci. USA* **117**, 32386 (2020).
- [18] Y. Hayakawa, M. Takaue, K. X. Ngo, T. Imai, M. D. Yamada, A. B. Behjat, K. Umeda, K. Hirose, A. Yurtsever, N. Kodera, K. Tokuraku, O. Numata, T. Fukuma, T. Ando, K. Nakano, and T. Q. Uyeda, Actin-binding domain of Rng2 sparsely bound on F-actin strongly inhibits actin movement on myosin II, *Life Sci. Alliance* **6**, e202201469 (2022).
- [19] K. X. Ngo, H. T. Vu, K. Umeda, M. N. Trinh, N. Kodera, and T. Uyeda, Deciphering the actin structure-dependent preferential cooperative binding of cofilin, *eLife* **13**, RP95257 (2024).
- [20] A. Kodan, R. Amyot, K. Umeda, F. Ogasawara, Y. Kimura, N. Kodera, and K. Ueda, Direct Visualization of ATP-Binding Cassette Protein A1 Mediated Nascent High-Density Lipoprotein Biogenesis by High-Speed Atomic Force Microscopy, *Nano Lett.* **25**, 13563 (2025).
- [21] S. J. Rupitsch, *Piezoelectric Sensors and Actuators: Fundamentals and Applications*

(Springer Berlin, Heidelberg, 2019).

- [22] Y. K. Yong, S. O. R. Moheimani, B. J. Kenton, and K. K. Leang, Invited Review Article: High-speed flexure-guided nanopositioning: Mechanical design and control issues, *Rev. Sci. Instrum.* **83**, 121101 (2012).
- [23] Y. K. Yong, Preloading Piezoelectric Stack Actuators in High-Speed Nanopositioning Systems, *Front. Mech. Eng.* **2**, 8 (2016).
- [24] M. P. Yothers, A. E. Browder, and L. A. Bumm, Real-space post-processing correction of thermal drift and piezoelectric actuator nonlinearities in scanning tunneling microscope images, *Rev. Sci. Instrum.* **88**, 013708 (2017).
- [25] N. Hosseini, A. P. Nievergelt, J. D. Adams, V. T. Stavrov, and G. E. Fantner, A monolithic MEMS position sensor for closed-loop high-speed atomic force microscopy, *Nanotechnology* **27**, 135705 (2016).
- [26] Y. L. Tian, Y. Ma, K. K. Lu, M. X. Yang, X. L. Zhao, F. J. Wang, and D. W. Zhang, Modeling and control methodology for an XYZ micro manipulator, *Rev. Sci. Instrum.* **90**, 105007 (2019).
- [27] Y. D. Tao, H. X. Li, and L. M. Zhu, Hysteresis modeling with frequency-separation-based Gaussian process and its application to sinusoidal scanning for fast imaging of atomic force microscope, *Sensor. Actuat. A-Phys.* **311**, 112070 (2020).
- [28] A. J. Fleming and S. O. R. Moheimani, Sensorless vibration suppression and scan

compensation for piezoelectric tube nanopositioners, *IEEE Trans. Control Syst. Technol.* **14**, 33 (2006).

- [29] M. Kageshima, S. Togo, Y. J. Li, Y. Naitoh, and Y. Sugawara, Wideband and hysteresis-free regulation of piezoelectric actuator based on induced current for high-speed scanning probe microscopy, *Rev. Sci. Instrum.* **77**, 103701 (2006).
- [30] A. J. Fleming and K. K. Leang, Charge drives for scanning probe microscope positioning stages, *Ultramicroscopy* **108**, 1551 (2008).
- [31] S. O. R. Moheimani and Y. K. Yong, Simultaneous sensing and actuation with a piezoelectric tube scanner, *Rev. Sci. Instrum.* **79**, 073702 (2008).
- [32] T. Kos, T. Rojac, J. Petrovcic, and D. Vrancic, Control system for automated drift compensation of the stand-alone charge amplifier used for low-frequency measurement, *AIP Adv.* **9**, 035133 (2019).
- [33] D. W. Song and C. J. Li, Modeling of piezo actuator's nonlinear and frequency dependent dynamics, *Mechatronics* **9**, 391 (1999).
- [34] D. Croft, G. Shed, and S. Devasia, Creep, hysteresis, and vibration compensation for piezoactuators: Atomic force microscopy application, *J. Dyn. Syst. Meas. Control* **123**, 35 (2001).
- [35] G. M. Clayton, S. Tien, K. K. Leang, Q. Z. Zou, and S. Devasia, A Review of Feedforward Control Approaches in Nanopositioning for High-Speed SPM, *J. Dyn. Syst. Meas. Control*

**131**, 061101 (2009).

[36] K. K. Leang, Q. Z. Zou, and S. Devasia, Feedforward Control of Piezoactuators in Atomic Force Microscope Systems, *IEEE Control Syst. Mag.* **29**, 70 (2009).

[37] H. Lu, Y. C. Fang, X. Ren, and X. B. Zhang, Improved direct inverse tracking control of a piezoelectric tube scanner for high-speed AFM imaging, *Mechatronics* **31**, 189 (2015).

[38] Veeco MultiMode SPM Instruction Manual,  
[https://www.cigs.unimo.it/cigsdownloads/labs/afm2/manuali\\_lettura/multimode\\_manual\\_revB.pdf](https://www.cigs.unimo.it/cigsdownloads/labs/afm2/manuali_lettura/multimode_manual_revB.pdf)  
(Accessed December 1, 2025)

[39] Agilent Technologies 5500 Scanning Probe Microscope User's Guide,  
[https://afmhelp.com/docs/manuals/agilent\\_5500\\_user\\_manual\\_revB.pdf](https://afmhelp.com/docs/manuals/agilent_5500_user_manual_revB.pdf) (Accessed December 1, 2025)

[40] J. Fu, W. Chu, R. Dixson, G. Orji, and T. Vorburger, Correction of Hysteresis in SPM Images by a Moving Window Correlation Method, *AIP Conf. Proc.* **1173**, 280 (2009).

[41] L. S. Zhang, X. B. Chen, J. C. Huang, H. L. Li, L. J. Chen, and Q. X. Huang, A method to correct hysteresis of scanning probe microscope images based on a sinusoidal model, *Rev. Sci. Instrum.* **90**, 023704 (2019).

[42] T. Dickbreder, F. Sabath, L. Höltkemeier, R. Bechstein, and A. Kühnle, unDrift: A versatile software for fast offline SPM image drift correction, *Beilstein J. Nanotech.* **14**, 1225 (2023).

[43] S. Kubo, K. Umeda, N. Kodera, and S. Takada, Removing the parachuting artifact using

two-way scanning data high-speed atomic force microscopy, *Biophys. Physicobiology* **20**, e200006 (2023).

- [44] A. K. Bain and P. Chand, *Ferroelectrics: Principles and Applications* (Wiley - VCH Verlag GmbH & Co. KGaA, 2017).
- [45] D. Meier and S. M. Selbach, Ferroelectric domain walls for nanotechnology, *Nat. Rev. Mater.* **7**, 157 (2022).
- [46] F. Oling, W. Bergsma-Schutter, and A. Brisson, Trimers, dimers of trimers, and trimers of trimers are common building blocks of annexin A5 two-dimensional crystals, *J. Struct. Biol.* **133**, 55 (2001).
- [47] H. Jung and D. G. Gweon, Creep characteristics of piezoelectric actuators, *Rev. Sci. Instrum.* **71**, 1896 (2000).
- [48] I. Horcas, R. Fernandez, J. M. Gomez-Rodriguez, J. Colchero, J. Gomez-Herrero, and A. M. Baro, WSXM: A software for scanning probe microscopy and a tool for nanotechnology, *Rev. Sci. Instrum.* **78**, 013705 (2007).
- [49] S. Fukuda and T. Ando, Faster high-speed atomic force microscopy for imaging of biomolecular processes, *Rev. Sci. Instrum.* **92**, 033705 (2021).
- [50] K. Umeda, Y. Kurokawa, Y. Murayama, and N. Kodera, Submolecular video-imaging of the Smc5/6 complex topologically bound to DNA, *bioRxiv*, 2025.08.15.670630 (2025).